

## RESEARCH ARTICLE

View Article Online  
View Journal | View IssueCite this: *Inorg. Chem. Front.*, 2026, **13**, 45

# A polar rotor for designing antiferroelectricity–antiferromagnetism in a quasi-2D organic–inorganic hybrid perovskite

Zi-Ao Qiu,<sup>a</sup> Hua-Kai Li,<sup>a</sup> Ze-Jiang Xu,<sup>a</sup> Liang-Han Shen,<sup>a</sup> Xiang Zhang,<sup>a</sup> Chao Shi,<sup>a</sup> Na Wang,<sup>a</sup> Xiao-Bin Fu,<sup>b</sup> Nian-Tao Yao,<sup>b</sup> Heng-Yun Ye<sup>a</sup> and Le-Ping Miao<sup>\*a</sup>

Antiferroelectric–antiferromagnetic (AFE–AFM) multiferroic materials have received extensive attention due to their applications in high-energy storage devices. However, achieving AFE–AFM properties in a hybrid molecular material is particularly challenging, because electric dipole orders and magnetic dipole orders are often mutually exclusive. Here, we report a molecular strategy that utilizes polar rotors combined with magnetic modules to overcome the above exclusion in a quasi-two-dimensional (Q-2D) hybrid perovskite platform. Based on non-ferroic [CBA]<sub>2</sub>CoCl<sub>4</sub> (CBA = cyclobutylammonium, CBC), F-substituted [DFCBA]<sub>2</sub>CoCl<sub>4</sub> (DFCBA = 3,3-difluorocyclobutylamine, DFCBC) with polar rotors shows AFE–AFM properties. Systematic experimental results reveal that the freezing of rotor movement forms antiparallel arranged dipole arrays, which is the origin of the AFE feature. Moreover, DFCBC exhibits antiferromagnetism from the inorganic [CoCl<sub>4</sub>]<sup>2–</sup> component, reaching 1.73Nβ at 50 kOe. Our study presents the advantages of the Ruddlesden–Popper (RP) hybrid perovskite molecular rotor platform for realizing AFE–AFM properties. It gives insight into the molecular design for controlling the macroscopic physical properties.

Received 11th July 2025,  
Accepted 8th October 2025  
DOI: 10.1039/d5qi01473e

rsc.li/frontiers-inorganic

## Introduction

In recent years, organic–inorganic hybrid perovskite (OIHP) materials have garnered significant attention for exploring ferroic materials due to their structural tunability, environmental benignity, and easy processability.<sup>1,2</sup> Multiferroicity refers to the coexistence of ferroelectricity, antiferroelectricity, antiferromagnetism, or ferroelasticity. AFE–AFM materials have emerged as promising candidates for next-generation energy storage applications.<sup>3–6</sup> AFE behavior commonly arises from the antiparallel alignment of adjacent dipoles. This leads to zero net polarization in the bulk phase. While under critical electric fields, it manifests as distinctive double *P–E* hysteresis loops.<sup>7–11</sup> AFM nature requires magnetic modules with lone-pair electrons to exhibit magnetic ordering.<sup>12–15</sup> However, the electric orders are exclusive to the magnetic orders. As a result, the coexistence of AFE and AFM properties remains a significant challenge.

The molecular rotor is an effective platform for achieving structural phase transitions (SPTs) in hybrid molecular

systems because thermal-activated rotational motions can trigger an order–disorder type phase transition.<sup>16–18</sup> A striking example is the supramolecular assembly of the molecular rotor [NH<sub>4</sub>(18-crown-6)]<sub>2</sub>[Mn(SCN)<sub>4</sub>], which shows a ferroelectric phase transition at 346 K through the motions of the rotor.<sup>19</sup> Furthermore, the rapid movement and reorientation of the polar rotors induce ferroic phase transitions in the 2D RP hybrid perovskite (TFCA)<sub>2</sub>CdCl<sub>4</sub> (TFCA = 2-fluoro-1-amino-pyrrolidinium).<sup>20</sup> Despite these advances, molecular rotor OIHP ferroic materials remain scarce, highlighting both a challenge and an opportunity for innovation in ferroic materials. Recent breakthroughs in OIHP have demonstrated remarkable progress in achieving ferroicity through the structural modification of organic cations.<sup>21–25</sup> Building on this progress, H/F substitution on organic cations has been shown to introduce polarity/chirality. This structural modification realizes polar arrays of the electric dipoles to induce ferroelectric/antiferroelectric performances. For example, through molecular assembly, the combination of the polar rotor 3,3-difluorocyclobutylammonium and [CuCl<sub>4</sub>]<sup>2–</sup> successfully yields a lead-free 2D OIHP material exhibiting ferroelectric properties.<sup>26</sup> Therefore, H/F substitution on the rotors resulting in polar rotor arrays is an effective approach for inducing ferroicity in the RP hybrid perovskite family.

Given the distinctive advantages of polar rotor structures, incorporating magnetic components will represent an effective

<sup>a</sup>Chaotic Matter Science Research Center, International Institute for Innovation, Jiangxi University of Science and Technology, Ganzhou 341000, P.R. China.  
E-mail: miaoleping@jxust.edu.cn

<sup>b</sup>National Key Laboratory of Thorium Energy, Shanghai Institute of Applied Physics, Chinese Academy of Science, Shanghai, 201800, China

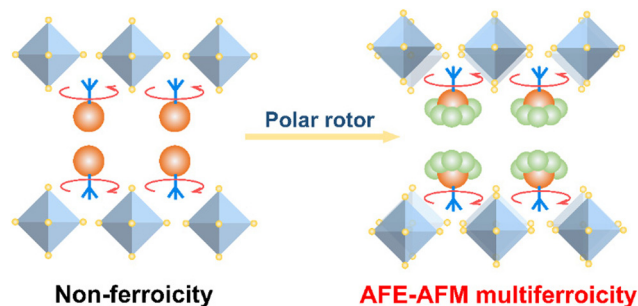
synthesis strategy to achieve magnetic multiferroicity. Here, based on the non-ferroic Q-2D RP hybrid perovskite CBC ( $[(\text{CBA})_2\text{CoCl}_4]$ ), DFCBC ( $[(\text{DFCBA})_2\text{CoCl}_4]$ ) was obtained, containing polar rotor arrays in the 2D van der Waals (vdW) layer by H/F substitution on the nonpolar symmetrical rotor of CBC (Scheme 1). DFCBC displays AFE properties due to the antiparallel arrangement of the polar rotor. Furthermore, DFCBC shows antiferromagnetism with  $1.73N\beta$  at 50 kOe because of the magnetic  $[\text{CoCl}_4]^{2-}$ . The results reveal the antiferroelectric–antiferromagnetic multiferroicity of DFCBC. This work presents the advantages of polar rotor arrays for designing AFE properties but also provides a simple and feasible approach for realizing magnetic multiferroic materials.

## Results and discussion

### Structural phase transition

Transparent block-shaped single crystals DFCBC and DFCBZ ( $[(\text{DFCBA})_2\text{ZnCl}_4]$ ) (Fig. S1) were synthesized *via* slow solvent evaporation. Subsequent characterization validated that the pure phase was verified by powder X-ray diffraction (PXRD), revealing excellent agreement between experimental and simulated patterns (Fig. S2). Thermogravimetry (TG) analysis confirmed structural integrity within this operational temperature regime, with no detectable mass loss observed below Curie temperature ( $T_c$ ) (Fig. S3).

To verify the reversible SPT of DFCBC and DFCBZ, differential scanning calorimetry (DSC) was systematically performed by comparing CBC (Fig. S4a) and CBZ (Fig. S4b) to F-substitution DFCBC (Fig. 1a) and DFCBZ (Fig. 1b), respectively. CBC and CBZ did not exhibit reversible thermal anomalies before melting, but DFCBC respectively displayed two endothermic/exothermic peaks at 359/350 K and 488/398 K, and the material exhibits thermal hysteresis of 9 K and 90 K. Similarly, DFCBZ showed a pair of peaks at 355 K and 348 K in heating–cooling cycles and exhibited thermal hysteresis of 7 K, which suggests an order–disorder phase transition.<sup>27–30</sup> DSC results indicate that the material is susceptible to SPT due to the incorporation of polar rotors. Thermodynamic analysis revealed an enthalpy change ( $\Delta H$ ) during the testing process, corresponding to an entropy



**Scheme 1** The polar rotor strategy for designing multiferroicity in the Q-2D RP hybrid perovskite system.

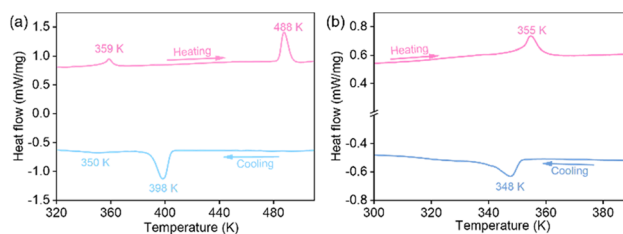


**Fig. 1** (a) DSC curves of DFCBC at 320–490 K. (b) DSC curves of DFCBZ at 300–390 K.

change ( $\Delta S$ ) as calculated *via*  $\Delta S = \Delta H/T$ ; by applying Boltzmann's relation  $\Delta S = R \ln N$ , the derived number of molecular orientations  $N$  (2.42 (Note S1) and 2.85 (Note S2)) suggests an order–disorder phase transition, consistent with the result observed in DSC analysis.

### Crystal structures

To reveal the Q-2D perovskite structure of DFCBC and DFCBZ (Fig. S5), variable-temperature single-crystal X-ray diffraction (SCXRD) was performed. At 300 K in the LTP (Fig. 2a), DFCBC crystallizes in the monoclinic system  $P2_1/n$  space group with unit cell parameters  $a = 11.9748(7)$  Å,  $b = 11.3663(7)$  Å,  $c = 24.1353(14)$  Å,  $\alpha = 90^\circ$ ,  $\beta = 91.858(5)^\circ$ ,  $\gamma = 90^\circ$ , and  $V = 3283.3(3)$  Å<sup>3</sup>. The minimum asymmetric unit, which comprises the DFCBA cation and the  $[\text{CoCl}_4]^{2-}$  anion, exhibits an ordered arrangement (Fig. 2a). This antiparallel arrangement of organic cations has no polarity, which is the molecular basis of AFE.<sup>31</sup>

At 383 K in the HTP, the space group of DFCBC is changed to  $P2_1/c$  with unit cell parameters  $a = 12.2354(8)$  Å,  $b = 11.5412(8)$  Å,  $c = 11.9953(8)$  Å,  $\alpha = 90^\circ$ ,  $\beta = 92.485(6)^\circ$ ,  $\gamma = 90^\circ$ , and  $V = 1692.3(2)$  Å<sup>3</sup>. Notably, a comparison of the unit cell parameters at the LTP and HTP revealed that DFCBC exhibits the characteristic AFE-PE phase transition, characterized by a significant decrease in both

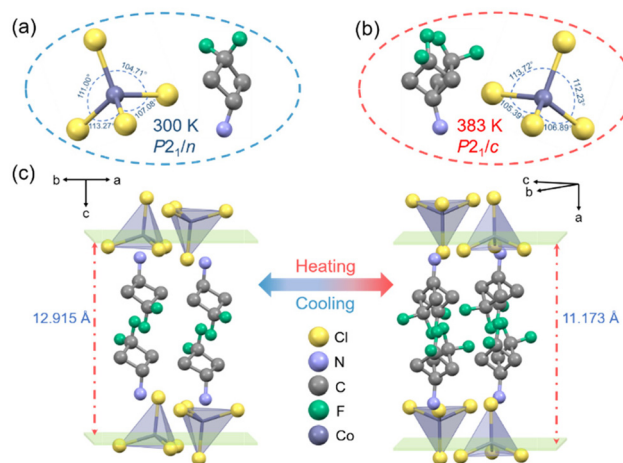


**Fig. 2** The molecular structural packing model in (a) the LTP and (b) the HTP of DFCBC. (c) Structural changes of DFCBC between the LTP and HTP.

the axis and volume in one direction.  $[\text{CoCl}_4]^{2-}$  shows a slight distortion with changes in bond lengths and angles (Fig. 2b). Affected by the temperature, the inorganic interlayer spacing decreased from 12.915 Å to 11.173 Å (Fig. 2c). Furthermore, thermally activated rotational dynamics enable the polar molecular rotor to overcome its energy barrier within the inorganic framework, inducing dynamic disorder of cationic arrangements by rapid reorientation processes.<sup>32,33</sup> In the LTP and HTP, the experimental PXRD patterns exhibit nearly identical features, which is the same as the result of comparing the simulated patterns. As shown in Fig. S6, no significant alterations are observed in the PXRD patterns before and after the phase transition. This may be attributed to DFCBC undergoing an isomorphous phase transition.

For the compound DFCBZ, at 300 K and 373 K, the crystal-line space group changed from  $P2_1/n$  to  $P2_1/c$ , representing an isostructural phase transition, and the inorganic frame is distorted at 373 K (Fig. S7). Additionally, the unit cell parameters of DFCBZ also conform to the AFE phase transition characteristics. The possibility of AFE regulation by polar rotors was further verified by testing crystal structures.

### Dynamics of the polar rotor

The dynamic behavior of the molecular rotor in DFCBZ was systematically investigated using variable-temperature solid-state nuclear magnetic resonance (ss-NMR) spectroscopy. Variable-temperature  $^{13}\text{C}$  cross-polarization/magic angle spinning (CP/MAS) NMR spectroscopy revealed distinct molecular motions associated with crystal structure alteration. At 293 K, three resolved resonances were observed at 36.87, 43.57, and 121.14 ppm, corresponding to the C1, C2/C4 (same signal), and C3 sites of the rotor, respectively (Fig. 3a). Notably, the spectral features remained unchanged below 333 K, indicating thermally restricted rotational dynamics of the organic rotor. Upon approaching the critical  $T_c$ , a pronounced narrowing of the C2/C4 signal was observed (Fig. 3b), signifying a dramatic increase in molecular thermal motion, consistent with reduced hydrogen-bonding interactions (N–H...Cl) as evidenced by crystallographic data. In contrast, C1 and C3 signals exhibited minimal temperature-dependent shifts,

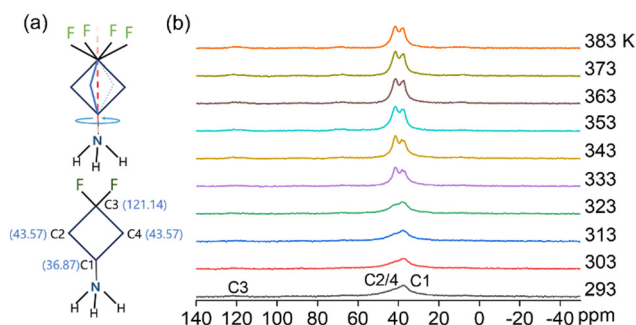


**Fig. 3** (a) The rotating motion mode and C atoms labeling with the corresponding chemical shift of the polar rotor DFCBZ. (b)  $^{13}\text{C}$  CP/MAS NMR spectra of DFCBZ around 293–383 K.

suggesting motions along the central axis of the organic molecule itself. These dynamics of site-specific imply that thermally activated reorientation of the organic component occurs preferentially about the polar axis, driving the SPT.

### Dielectric response and antiferroelectric

Dielectric properties represent the macro-response of a material to external stimuli (electric fields, temperature, or stress). SPT often manifests as anomalous dielectric behavior, with significant variations in permittivity under thermal activation. The complex dielectric constant can be expressed as  $\epsilon_r = \epsilon' - i\epsilon''$ , where  $\epsilon'$  quantifies the real part and  $\epsilon''$  reflects the imaginary part. Variable-temperature dielectric measurements of DFCBC at 1 MHz (310–370 K) revealed a sharp transition between distinct dielectric states (Fig. 4a). Below  $T_c$ , the low-dielectric state exhibited  $\epsilon' \approx 30$ , which surged abruptly to 92.3 in the high-dielectric state near  $T_c$ , displaying a characteristic sharp peak-like anomaly. As the measurement frequency increases from 0.5 kHz to 1 MHz (Fig. S8a), the peak  $\epsilon'$  rises from 92.3 to 348 while simultaneously exhibiting frequency-dependent attenuation. The transition temperature aligns precisely with DSC results. Subsequently, the dielectric measurements of DFCBZ (Fig. 4b) were carried out under these conditions, and the typical sharp peak-like anomaly was observed near  $T_c$ . Furthermore, as shown in Fig. S8b, with the change of frequency, DFCBZ exhibits dielectric relaxation. This behavior provides direct evidence for the feasibility of polar rotors regulating SPT.

The nonlinear  $P$ - $E$  hysteresis serves as a defining characteristic for identifying AFE materials. Variable-temperature polarization measurements of DFCBC demonstrate characteristic AFE phase transition behavior. The material attains a maximum polarization ( $P_{\text{max}}$ ) of  $2.061 \mu\text{C cm}^{-2}$  under  $E_{\text{max}} = 1.66 \text{ kV cm}^{-1}$ , with two symmetric hysteresis loops

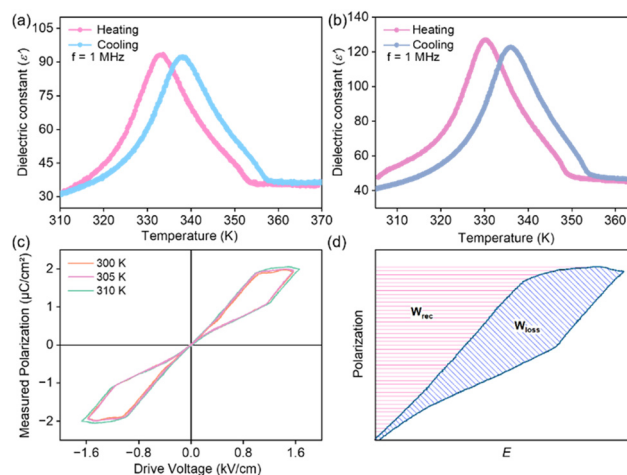


**Fig. 4** Temperature-dependent curves of  $\epsilon'$  at 1 MHz frequency of (a) DFCBC and (b) DFCBZ. (c) Temperature dependence of  $P$ - $E$  hysteresis loops at 50 Hz. (d) The schematic diagram for the calculation of the energy storage properties of antiferroelectric materials at 310 K.

emerging when exceeding critical electric fields below  $T_c$  (Fig. 4c). The spontaneous reorientation of antiparallel dipoles driven by energy minimization leads to near-zero residual polarization ( $P_r$ ), characteristic of AFE ground state recovery. In addition, the recoverable energy density ( $W_{\text{rec}}$ ) and energy efficiency ( $\eta$ ) constitute critical figures of merit for evaluating practical energy storage performance (Fig. 4d).  $W_{\text{rec}}$  (red integration area) can be calculated using  $W_{\text{rec}} = \int_{P_r}^{P_{\text{max}}} E dP$  (where  $P_{\text{max}}$  is the maximum polarization value and  $P_r$  is the residual polarization value). The energy efficiency  $\eta = \frac{W_{\text{rec}}}{W_{\text{rec}} + W_{\text{loss}}}$  (where  $W_{\text{loss}}$  is the energy loss) reaches 57.50% at 310 K.<sup>34</sup> Notably, the energy storage efficiency of DFCBZ (Fig. S9) is 70.76% from the above calculation.

### Antiferromagnetic properties

The magnetic properties of the compound DFCBC were systematically investigated through direct current (DC) magnetic susceptibility measurements performed on powdered samples under an applied field of 1 kOe across a broad temperature range (2–400 K).

As depicted in Fig. 5a and S10, temperature-dependent measurements of the molar magnetic susceptibility ( $\chi_M$ ) and  $\chi_M T$  product were conducted at a controlled heating rate of 3 K  $\text{min}^{-1}$ . The  $\chi_M T$  product demonstrates a pronounced increase from 1.6  $\text{cm}^3 \text{K mol}^{-1}$  at 35 K to a maximum value of 1.96  $\text{cm}^3 \text{K mol}^{-1}$  at 400 K, indicative of significant antiferromagnetic coupling between the metal centers. This temperature-dependent magnetic behavior is in excellent agreement with previously reported antiferromagnetic systems.<sup>35–38</sup>

Quantitative analysis of the magnetic susceptibility data through Curie–Weiss fitting over the entire temperature range (2–400 K) yields a Curie constant ( $C$ ) of 2.0  $\text{cm}^3 \text{K mol}^{-1}$  and a negative Weiss temperature ( $\theta = -13.98 \text{ K}$ ), providing further compelling evidence for dominant antiferromagnetic interactions. Complementary isothermal magnetization measurements (Fig. 5b) exhibit a characteristic gradual increase in magnetization with the applied field, reaching  $1.73N\beta$  at 50 kOe. Notably, this magnetization value is significantly lower than the theoretical spin-only value ( $M = gS_{\text{Co}} = 3.0N\beta$ ), consistent with the antiferromagnetic ground state of the compound.

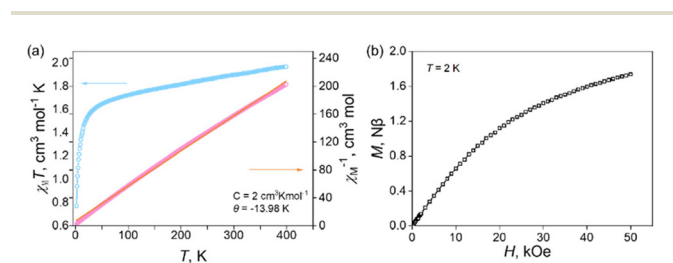


**Fig. 5** (a) Temperature-dependent susceptibilities under a dc field of 1 kOe and Curie–Weiss fitted curves for DFCBC. (b) Field-dependent isothermal magnetization ( $M$ ) at 2 K.

## Conclusions

In summary, we successfully synthesized a Q-2D RP AFE hybrid perovskite using a polar rotor strategy. The thermally driven rotational motions of the polar rotor are the molecular origin of the AFE phase transition. Besides, the magnetic framework  $[\text{CoCl}_4]^{2-}$  results in AFM properties. The combination of the polar rotor structure and magnetic component overcomes the repulsive effects of the electric dipole orders and the magnetic dipole orders. Our study reveals that the RP hybrid perovskite systems with polar rotors offer a good platform to realize AFE–AFM multiferroic behavior, providing an in-depth perspective to design molecular functional materials.

## Author contributions

L. P. M. conceived the project. Z. A. Q. prepared the compound. X. B. F. measured and analysed the solid-state NMR spectra. Z. J. X., H. K. L. and L. H. S. prepared the samples and performed the DSC, PXRD, TG and dielectric measurements. X. Z. and C. S. contributed to the single crystal measurement and analysis. N. T. Y. and H. Y. Y. performed the antiferroelectric and antiferromagnetic characterization. L. P. M. and N. W. wrote the manuscript, with inputs from all other authors.

## Conflicts of interest

There are no conflicts to declare.

## Data availability

The datasets supporting this article have been uploaded as part of the supplementary information (SI). Supplementary information is available. See DOI: <https://doi.org/10.1039/d5qi01473e>.

CCDC 2450180–2450185 contain the supplementary crystallographic data for this paper.<sup>39a–f</sup>

## Acknowledgements

L.-P. M. acknowledges the support from the National Natural Science Foundation of China (Grant No. 22205087 and 22371095) and the Natural Science Foundation of Jiangxi Province (Grant No. 20232BAB213003 and 20242BAB23015). N. W. acknowledges the support from the Science and Technology Project of Jiangxi Provincial Department of Education (Grant No. GJJ2400711) and the China Postdoctoral Science Foundation (Grant No. 2024M761225). H.-Y. Y. acknowledges the support from the National Natural Science Foundation of China (Grant No. 22275075) and the Natural Science Foundation of Jiangxi Province (Grant No. 20204BCJ22015).

## References

- M. L. Ren, W. Luo, Z. J. Xu, H. K. Li, L. Liu, C. Shi, N. Wang, H. Y. Ye and L. P. Miao, H/OH substitution achieving high-temperature multiferroicity in a Sn(IV)-based hybrid perovskite, *Inorg. Chem. Front.*, 2024, **11**, 7617–7622.
- Z. J. Xu, W. Luo, H. K. Li, M. L. Ren, C. Shi, N. Wang, H. Y. Ye and L. P. Miao, Multiaxial Multiferroicity with Large Spontaneous Polarization in a Hydroxyl-Modified Quinuclidinium Gallium(III) Chloride, *Chem. Mater.*, 2024, **36**, 7595–7603.
- P. F. Li, W. Q. Liao, Y. Y. Tang, H. Y. Ye, Y. Zhang and R. G. Xiong, Unprecedented Ferroelectric-Antiferroelectric-Paraelectric Phase Transitions Discovered in an Organic-Inorganic Hybrid Perovskite, *J. Am. Chem. Soc.*, 2017, **139**, 8752–8757.
- S. G. Han, X. T. Liu, Y. Liu, Z. Y. Xu, Y. B. Li, M. C. Hong, J. H. Luo and Z. H. Sun, High-Temperature Antiferroelectric of Lead Iodide Hybrid Perovskites, *J. Am. Chem. Soc.*, 2019, **141**, 12470–12474.
- L. S. Gao, H. Z. Guo, S. J. Zhang and C. A. Randall, A perovskite lead-free antiferroelectric  $x\text{CaHfO}_3\text{-(1-x)NaNbO}_3$  with induced double hysteresis loops at room temperature, *J. Appl. Phys.*, 2016, **120**, 204102.
- A. A. Belik, Hybrid Multiferroic Behavior in the Double Perovskite  $(\text{Ca}_{0.5}\text{Mn}_{1.5})\text{MnWO}_6$ , *Chem. Mater.*, 2024, **36**, 7604–7609.
- H. J. Xu, W. Q. Guo, J. Q. Wang, Y. Ma, S. G. Han, Y. Liu, L. Lu, X. Pan, J. H. Luo and Z. H. Sun, A Metal-Free Molecular Antiferroelectric Material Showing High Phase Transition Temperatures and Large Electrocaloric Effects, *J. Am. Chem. Soc.*, 2021, **143**, 14379–14385.
- Z. X. Wang, Y. Zhang, Y. Y. Tang, P. F. Li and R. G. Xiong, Fluorination Achieved Antiperovskite Molecular Ferroelectric in  $(\text{CH}_3)_2(\text{F}-\text{CH}_2\text{CH}_2)\text{NH}_3(\text{CdCl}_3)(\text{CdCl}_4)$ , *J. Am. Chem. Soc.*, 2019, **141**, 4372–4378.
- Z. J. Xu, N. Wang, W. Luo, H. K. Li, Y. Feng, C. Shi, H. Y. Ye and L. P. Miao, Crystal Sponge Behavior in a Two-Dimensional Rare-Earth Hybrid Coordinate Polymer, *Inorg. Chem.*, 2023, **62**, 13937–13942.
- S. K. Thatikonda, W. H. Huang, X. R. Du, C. Y. Yao, Y. F. Ke, J. Wu, N. Qin and D. H. Bao, Ti-doping induced antiferroelectric to ferroelectric phase transition and electrical properties in Sm-PbZrO<sub>3</sub> thin films, *Curr. Appl. Phys.*, 2021, **24**, 12–18.
- X. Q. Li, Z. S. Yue, F. Zhang, Q. X. Wang, Q. Y. Wei, Z. H. Sun, J. H. Luo and X. T. Liu, Stereo-Active Lone Pairs Induced Giant Polarization in a 2D Ge-Based Halide Perovskite Antiferroelectric, *Adv. Funct. Mater.*, 2024, **34**, 2311944.
- M. Z. Li, D. Han, Z. H. Wang, B. Li, T. Yang, Z. Zhang, F. Gao, H. Wang, X. G. Zhao, D. Li and Z. D. Zhang, Magnetic and transport properties in antiferromagnetic antiperovskite Eu<sub>3</sub>SnO, *Phys. Rev. Mater.*, 2023, **7**, 074203.
- E. Blackburn, CONDENSED-MATTER PHYSICS Antiferromagnetism with a twist, *Nat. Phys.*, 2019, **15**, 625–626.
- Y. H. Xu, Z. H. Tan, W. T. Chen, C. K. Chang, Y. C. Chuang, M. Goto and Y. Shimakawa, High-Pressure Synthesized Perovskite CdMnO<sub>3</sub> with C-Type Antiferromagnetic Spin Configuration, *Inorg. Chem.*, 2022, **61**, 21011–21015.
- D. B. Straus, T. Klimczuk, X. H. Xu and R. J. Cava, Antiferromagnetic Order in the Rare-Earth Halide Perovskites CsEuBr<sub>3</sub> and CsEuCl<sub>3</sub>, *Chem. Mater.*, 2022, **34**, 10772–10777.
- B. Y. Wang, C. T. He, B. Huang, W. J. Xu, W. Xue, Z. Y. Du, W. X. Zhang and X. M. Chen, Thermal-induced reversible ferroelastic phase transition in a new bromethyl-substituted molecular rotor, *Sci. China: Chem.*, 2015, **58**, 1137–1143.
- Z. X. Zhang, T. Zhang, P. P. Shi, W. Y. Zhang, Q. Ye and D. W. Fu, Anion-Regulated Molecular Rotor Crystal: The First Case of a Stator-Rotator Double Switch with Relaxation Behavior, *J. Phys. Chem. Lett.*, 2019, **10**, 4237–4244.
- Y. B. Tong, Z. F. Tian, H. B. Duan, Z. P. Zhu, T. Y. Hong and J. K. Yang, Monocycle-like Molecular Rotor Induces a Dielectric Relaxation and Dielectric Phase Transformation in an Organic-Inorganic Hybrid Supermolecule, *Eur. J. Inorg. Chem.*, 2018, **29**, 3427–3432.
- N. Wang, H. K. Li, H. Y. Shen, L. Ye, Z. J. Xu, M. L. Ren, N. T. Yao, C. Shi, H. Y. Ye and L. P. Miao, Supramolecular Rotor Assembly for the Design of a Hybrid Ferroelectric-Antiferromagnetic Multiferroic Semiconductor, *Angew. Chem., Int. Ed.*, 2025, **10**, e202421298.
- W. Luo, N. Wang, H. K. Li, Z. J. Xu, Y. Feng, X. B. Fu, C. Shi, H. Y. Ye and L. P. Miao, Fast rotating dipole array inducing large dielectric response in a Ruddlesden-Popper hybrid perovskite ferroelastic, *Inorg. Chem. Front.*, 2023, **10**, 5082–5088.
- M. Tahir, X. X. Feng, Y. H. Li, J. Q. Gao, F. Aslam, M. I. Sadiq, B. Liu and J. L. Yang, Surface modification in FAPbI<sub>3</sub> perovskites using methyl-substituted benzene derivatives: impact of functional groups and methyl position, *Phys. Scr.*, 2025, **100**, 035949.
- G. Q. Cheng, J. Wang, R. Yang, C. Li, H. Zhang, N. N. Wang, R. Z. Li, J. P. Wang and W. Huang, Tuning crystal orientation and charge transport of quasi-2D perovskites via halogen-substituted benzylammonium for efficient solar cells, *J. Energy Chem.*, 2022, **66**, 205–209.
- L. P. Long, Z. W. Huang, Z. K. Xu, T. Gan, Y. Qin, Z. W. Chen and Z. X. Wang, H/F substitution activating tunable dimensions and dielectric-optical properties in organic lead-bromide hybrids, *Inorg. Chem. Front.*, 2024, **11**, 845–852.
- M. Y. Wan, W. F. Liu, J. L. Luo, J. Liao, F. X. Wang, L. J. Wang, Y. Z. Tang and Y. H. Tan, Silver/Antimony-Base Multifunctional Double Perovskite with H/F Substitution Enhance Properties, *Inorg. Chem.*, 2024, **63**, 3083–3090.
- Y. Y. Tang, Y. Ai, W. Q. Liao, P. F. Li, Z. X. Wang and R. G. Xiong, H/F-Substitution-Induced Homochirality for

- Designing High- $T_c$  Molecular Perovskite Ferroelectrics, *Adv. Mater.*, 2019, **31**, 1902163.
- 26 C. R. Huang, X. Z. Luo, X. G. Chen, X. J. Song, Z. X. Zhang and R. G. Xiong, A multiaxial lead-free two-dimensional organic-inorganic perovskite ferroelectric, *Natl. Sci. Rev.*, 2021, **8**, nwa232.
- 27 Y. F. Huang, L. Xiang, Y. Feng, Z. An, L. P. Miao, J. R. Li, H. Y. Ye and C. Shi, High Quality of a Perchlorate-Based Hybrid Perovskite-Type Cage-Like Single Crystal-Evidence of Temperature-Induced Distinct Dielectric Transition, *Eur. J. Inorg. Chem.*, 2021, **43**, 4439–4442.
- 28 L. K. Wu, Q. H. Zou, H. Q. Yao, H. Y. Ye and J. R. Li, Zero-dimensional organic-inorganic hybrid manganese bromide with coexistence of dielectric-thermal double switches and efficient photoluminescence, *Dalton Trans.*, 2023, **52**, 11558–11564.
- 29 Y. D. Zhang, L. Ye, N. Wang, L. P. Miao, H. Y. Ye and C. Shi, Structural Diversity and Tunable Ferroelectricity in a Family of Hybrid Perovskites:  $AM(NO_3)_3$ , *Cryst. Growth Des.*, 2023, **23**, 5323–5329.
- 30 Z. Y. Yue, H. K. Li, N. Wang, S. S. Liu, L. P. Miao, H. Y. Ye and C. Shi, Dehydration-triggered structural phase transition-associated ferroelectricity in a hybrid perovskite-type crystal, *Chin. Chem. Lett.*, 2024, **35**, 109355.
- 31 N. Wang, Z. Shen, W. Luo, H. K. Li, Z. J. Xu, C. Shi, H. Y. Ye, S. Dong and L. P. Miao, Noncollinear ferroelectric and screw-type antiferroelectric phases in a metal-free hybrid molecular crystal, *Nat. Commun.*, 2024, **15**, 10262.
- 32 Y. F. Gao, Z. X. Zhang, T. Zhang, C. Y. Su, W. Y. Zhang and D. W. Fu, Regulated molecular rotor in phase transition materials with switchable dielectric and SHG effect, *Mater. Chem. Front.*, 2020, **4**, 3003–3012.
- 33 L. P. Miao, L. L. Chu, X. B. Han, B. D. Liang, C. Y. Chai, C. C. Fan, X. X. Wang, Y. F. Yao and W. Zhang, A ferroelastic molecular rotor crystal showing inverse temperature symmetry breaking, *Inorg. Chem. Front.*, 2021, **8**, 2809–2816.
- 34 Z. Y. Wu, X. T. Liu, C. M. Ji, L. N. Li, S. S. Wang, Y. Peng, K. W. Tao, Z. H. Sun, M. C. Hong and J. H. Luo, Discovery of an Above-Room-Temperature Antiferroelectric in Two-Dimensional Hybrid Perovskite, *J. Am. Chem. Soc.*, 2019, **141**, 3812–3816.
- 35 L. Zhao, Q. Liu, S. J. Zhang and J. F. Li, Lead-free  $AgNbO_3$  anti-ferroelectric ceramics with an enhanced energy storage performance using  $MnO_2$  modification, *J. Mater. Chem. C*, 2016, **4**, 8380–8384.
- 36 C. L. Jiang, Q. Q. Luo, H. M. Fu, H. C. Lin, C. H. Luo, J. L. Wang, X. J. Meng, H. Peng, C. G. Duan and J. H. Chu, Ferroelectricity and antiferromagnetism in organic-inorganic hybrid (1,4-bis(imidazol-1-ylmethyl)benzene)  $CuCl_4 \cdot H_2O$ , *CrystEngComm*, 2020, **22**, 587–592.
- 37 Y. Ai, R. Sun, Y. L. Zeng, J. C. Liu, Y. Y. Tang, B. W. Wang, Z. M. Wang, S. Gao and R. G. Xiong, Coexistence of magnetic and electric orderings in a divalent  $Cr^{2+}$ -based multi-axial molecular ferroelectric, *Chem. Sci.*, 2021, **12**, 9742–9747.
- 38 Y. Ai, R. Sun, W. Q. Liao, X. J. Song, Y. Y. Tang, B. W. Wang, Z. M. Wang, S. Gao and R. G. Xiong, Unprecedented Ferroelectricity and Ferromagnetism in a  $Cr^{2+}$ -Based Two-Dimensional Hybrid Perovskite, *Angew. Chem., Int. Ed.*, 2022, **61**, e202206034.
- 39 (a) CCDC 2450180: Experimental Crystal Structure Determination, 2025, DOI: [10.5517/ccdc.csd.cc2n7m2m](https://doi.org/10.5517/ccdc.csd.cc2n7m2m);  
 (b) CCDC 2450181: Experimental Crystal Structure Determination, 2025, DOI: [10.5517/ccdc.csd.cc2n7m3n](https://doi.org/10.5517/ccdc.csd.cc2n7m3n);  
 (c) CCDC 2450182: Experimental Crystal Structure Determination, 2025, DOI: [10.5517/ccdc.csd.cc2n7m4p](https://doi.org/10.5517/ccdc.csd.cc2n7m4p);  
 (d) CCDC 2450183: Experimental Crystal Structure Determination, 2025, DOI: [10.5517/ccdc.csd.cc2n7m5q](https://doi.org/10.5517/ccdc.csd.cc2n7m5q);  
 (e) CCDC 2450184: Experimental Crystal Structure Determination, 2025, DOI: [10.5517/ccdc.csd.cc2n7m6r](https://doi.org/10.5517/ccdc.csd.cc2n7m6r);  
 (f) CCDC 2450185: Experimental Crystal Structure Determination, 2025, DOI: [10.5517/ccdc.csd.cc2n7m7s](https://doi.org/10.5517/ccdc.csd.cc2n7m7s).